Journal of Ceramic Processing Research. Vol. 17, No. 8, pp. 870~875 (2016)

J O U R N A L O F
Ceramic Processing Research

Elaboration and characterization of barium titanate powders obtained by the mechanical activation of barium nitrate and titanate oxide, and electrical properties of the ceramics sintered by SPS

Tawfik Al-Naboulsi[a,b], Madona Boulos[a], Christophe Tenailleau[b], Pascal Dufour[b], Mirvat Zakhour[a] and Sophie Guillemet-Fritsch[b]

[a]*Laboratoire de Chimie Physique des Matériaux (LCPM, PR2N), EDST, Universit Libanaise, Faculté des Sciences II, Département de Chimie, Fanar, Liban*

[b]*Institut Carnot CIRIMAT, UMR CNRS 5085. Université Paul Sabatier. 118, route de Narbonne. 31062 Toulouse Cedex 09, France*

The current work aims to reduce the energy required to obtain a high quality barium titanate nanocrystals via solid-state reaction. In order to achieve this challenge, $Ba(NO_3)_2$ and TiO_2 were mechanically activated by high-energy ball milling, and then heat treated at moderate temperature (600 °C). When stoichiometric mixture was used, the formation of BT and minor $BaCO_3$ and TiO_2 impurities was observed. The use of $Ba(NO_3)_2$ excess leads to the formation of BT and a minor $BaCO_3$ impurity. A simple acid wash treatment was used to remove the carbonate impurity and to provide a high purity BT. The powders were characterized by XRD, BET, Raman spectroscopy, and SEM-FEG. Spark Plasma Sintering (SPS) technique was used to get the dense nanoceramics. These materials show, at room temperature and at 1 kHz, colossal permittivity ($\varepsilon = 10^5$) associated with low dielectric loss (tg $\delta = 0.07$).

Key words: Barium titanate, Mechanosynthesis, SPS, Electrical properties.

Introduction

$BaTiO_3$ is one of the most widely used dielectric materials for electronic application, especially in multilayers capacitors [1-3]. The electrical properties of $BaTiO_3$ highly depend on the structure, grain size, purity, etc... Different synthesis methods were powered to control the grain size and to produce high purity barium titanate like solid-state reaction [4], hydrothermal method [5, 6], sol-gel processing [7, 8], coprecipitation [9, 10], self-propagating high-temperature synthesis [11]. In particular, powders produced by hydrothermal synthesis or solution precipitation methods often contain hydroxyl groups that lead to the formation of undesired porosity during the elaboration of ceramics [4]. Therefore, there is an interest and a challenge for producing fine $BaTiO_3$ (BT) powders with narrow particle size distribution by solid-state reaction. The mechanical activation, as a top-down nanostructuring and large-scale technique, is considered as unsophisticated and low cost method [4, 12-19]. High-energy milling can greatly improve the reactivity of precursors, thereby reducing the phase formation temperature of BT [20]. Various barium and titanium precursors, like barium carbonate [4, 12-16, 21, 22], barium oxide [23], barium hydroxide [20], titanium oxide anatase and rutile [22], were used to produce BT by mechanical activation. However, in all cases, high temperature treatment or extreme synthesis conditions (e.g. high rotation speed [14], well controlled atmosphere [20]) are necessary to obtain the pure BT phase. The high temperature reactions often lead to powders presenting large particle size and wide particle size distribution. Therefore there is an interest to develop a low temperature, low cost, solid phase method for the preparation of nanocrystalline $BaTiO_3$ powders. To achieve this goal, new precursors are required. It has been reported that the anatase TiO_2, due to its low density and high surface energy [22, 24], is highly reactive and helps to lower the temperature of formation of BT. Furthermore, the high reactivity of barium nitrate is a great advantages to use it as a precursor. Therefore, $Ba(NO_3)_2$ and anatase TiO_2 were chosen as starting materials to produce BT powders using mechanical activation synthesis.

Spark Plasma Sintering (SPS) is the adapted tool for producing well densified ceramics with small grain size, due to short time of experiment, and lower sintering temperature, compared to the conventional sintering process [25]. Previous work has shown that the reductive atmosphere during the sintering of nano BT increases the number of charge carriers in ceramics, by the reduction of Ti^{4+} in Ti^{3+} thus creating high concentration of oxygen vacancies and electrons. The presence of a large number of point defects leads to colossal permittivity (ε') [10, 25, 26].

The present paper reports the synthesis of barium titanate, via mechanical activation, from barium nitrate

*Corresponding author:
Tel : +33(0)-5-61-55-62-83
Fax: +33(0)-5-61-55-61-33
E-mail: guillem@chimie.ups-tlse.fr

and anatase TiO_2, for the first time to our knowledge. For comparison, the formation of $BaTiO_3$ from barium carbonate and TiO_2 has been studied as well. Then, high-density nanostructured ceramics were elaborated by SPS.

Experimental

Sample preparation

$BaTiO_3$ powders were prepared from powders mixture of barium nitrate ($Ba(NO_3)_2$ (BN), Pro-analysis 99%) and titanium dioxide (TiO_2 (anatase), Acro-organic 99%) powders, that were mechanically milled at room temperature under air atmosphere in an alumina container, with a $Ba(NO_3)_2/TiO_2$ ratio of 1.05. Barium carbonate is from Merck (BaC, Pro-analysis 99%). The milling was performed during 8 hours using a Retsch PM 100 planetary apparatus at 350 rpm with a ball-to-powder weight ratio equal to 10 (alumina balls, = 10 mm). The obtained powders were then calcinated in air at 600 ºC for 1 hr. They were introduced -without binder- in an 8 mm graphite die. The die was placed in the SPS equipment (SPS Syntex Inc., Dr. Sinter 2080) for powder sintering at 1112 ºC during 3 min under 50 MPa of mechanical stress. A heating and a cooling rate of 24 ºC/min and 150 ºC/min, respectively, were used. Finally the obtained pellets were polished to remove the graphite layers (due to due to contamination from graphite foils. Sintered pellets were then post-annealed at 750 ºC for 15 min to induce partial re-oxidation and obtain the insulating characteristics of the ceramic samples.

Sample characterization

The oxide powder morphology was observed by the mean of a field electron gun scanning electron microscope (SEM-FEG, JEOL JSM 6700). The structure was identified by X-ray diffraction analysis. The data were collected on a Bruker D8 X-ray diffractometer (Cu Kα = 1.5418 Å) from 20 º to 80 º (2 theta). The Raman investigations were carried out by means of Horiba xploRATM. The powder specific surface area was measured by nitrogen desorption according to the BET method (micrometrics Desorb 2300A, Flow Sorb II 2300). Assuming that the powders are constituted of single-sized and non-porous spherical particles, their geometrical surface is related to the diameter by the relation S = 6/(d.l) (where S = BET specific surface area ($cm^2.g^{-1}$); d = particle diameter (cm) and l = the theoretical specific mass (6.02 $g.cm^{-3}$). The thermo-gravimetric analyses (TGA) were performed using a NAVAS INSTRUMENTS MMS-4000 thermo-balance. The ceramics densities were determined by the Archimede's method. The surface of cross-sectioned ceramic was imaged with the AFM (Agilent 5420) using contact mode. Prior to electrical measurements, the ceramic disks were coated with thin gold electrodes (thickness ~ 30 nm) by sputtering (108 Auto, Cressington Scientific Instruments, Watford, U.K.). The relative permittivity and the dielectric losses were obtained from impedance measurements using a 4294A Precision Impedance Analyzer (Agilent Technologies, Palo Alto, CA) in the range of 40 Hz to 100 kHz at room temperature and an applied ac voltage of 1 V.

Results and Discussion

Thermogravimetric analysis (TGA) has been performed on the commercial $Ba(NO_3)_2$ (i) powder, 8hrs milled $Ba(NO_3)_2$ (ii), the equimolar $Ba(NO_3)_2$ and TiO_2 powder mixture milled for 8hrs (iii). The TGA curves are shown in Fig. 1(a). A total weight loss of approximately 41 and 31% are detected on the TG curve of (i) and (ii), respectively. This weight loss observed during the heating is attributed to the NO_2 and O_2 gas released, according to the following equations:

$$Ba(NO_3)_2 \rightarrow BaO + 2NO_2 + \tfrac{1}{2}\, O_2 \quad \text{for (i) and (ii)} \quad (1)$$

$$Ba(NO_3)_2 + TiO_2 \rightarrow BaTiO_3 + 2NO_2 + \tfrac{1}{2}\, O_2 \quad \text{for (iii)} \quad (2)$$

The weight loss of the milled sample (ii) starts at

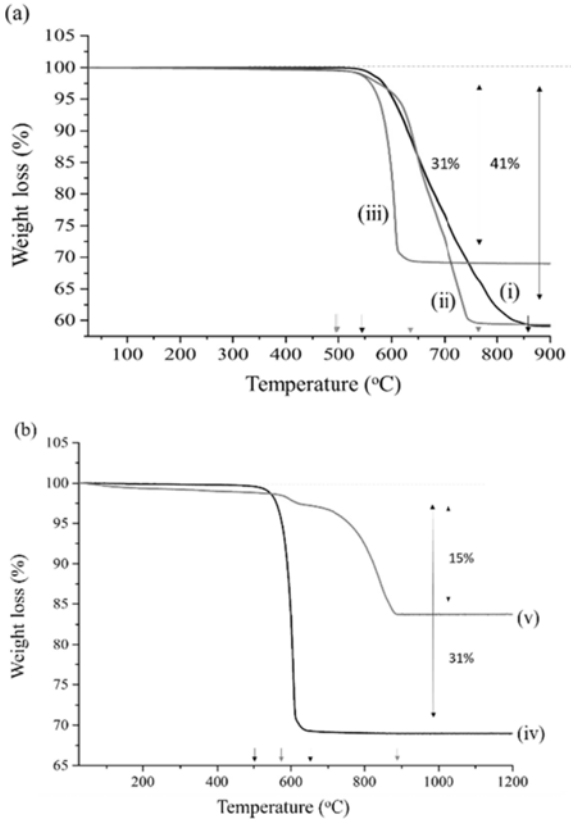

Fig. 1. TGA (in flowing air) of (a) commercial BN (i), 8h milled BN (ii) and BN and TiO_2 powder mixture milled during 8 hrs (iii) and (b) $Ba(NO_3)_2$ (iv) and $BaCO_3$ (v) milled with TiO_2 during 8 hrs.

500 °C and ends at 760 °C. Those temperatures are lower temperatures than the corresponding ones of the unmilled one (550 °C and 860 °C). Moreover, the milled $Ba(NO_3)_2$ powder presents a higher decomposition kinetics than the unmilled one. The higher reactivity of (ii) powder is explained by the decrease of the grain size after milling. Moreover, the addition of TiO_2 increases the kinetics of decomposition of $Ba(NO_3)_2$. Xue et al. [22, 27] have evidenced a catalytic effect of TiO_2 during the decomposition of $BaCO_3$ into CO_2 and $BaTiO_3$. In the present work, the TiO_2 anatase phases probably acts in the same way during the decomposition of $Ba(NO_3)_2$. The thermogravimetric studies have shown that both mechano-chemical activation and the catalysis effect of TiO_2 anatase are effective in the decrease of the decomposition reaction temperature of $Ba(NO_3)_2$ by almost 200 °C, compared to the composition without milling and without anatase phase TiO_2.

In order to show the advantage of using barium nitrate $Ba(NO_3)_2$ as a precursor instead of barium carbonate ($BaCO_3$), TGA were performed on $Ba(NO_3)_2$ (iv) and $BaCO_3$ (v) powders milled with TiO_2 for 8 hrs (Fig. 1(b)). The weight loss curves clearly indicate the decrease in the reaction temperature and the faster reaction kinetics in case of $Ba(NO_3)_2$ due to the low temperature decomposition and higher reactivity of the nitrate compared to carbonate.

Fig. 2 shows the XRD patterns of the $Ba(NO_3)_2$ and TiO_2 powder mixtures. Only the peaks corresponding to $Ba(NO_3)_2$ and TiO_2 were observed, indicating that no reaction has occurred. So a heat treatment is still required. The mixture has then been heat treated for 1 hr at 600 °C. All the peaks observed after calcination, are indexed in cubic perovskite structure (JCPDS file 31-174) of $BaTiO_3$. The crystalline size calculated from full width half-maximum (FWHM) using the Scherrer formula for the major (hkl) reflection is found to be ~ 25 nm. Additional peaks indicated the presence of a certain amount of $BaCO_3$ and anatase TiO_2 in the as-prepared powder. The non-reacted TiO_2 and the $BaCO_3$ phase persist even after the increasing of temperature (up to 700 °C or/and the duration of calcination (t = 6 hrs) (XRD not presented here). This result may be explained by the heterogeneity of the mixture after the fusion of $Ba(NO_3)_2$ during the calcination.

In order to remove the unwanted phases and because that barium excess phase (e.g: Ba_2TiO_4) is unstable below 700 °C (higher than the calcination temperature) [28], the Ba/Ti ratio has been increased to 1.05. In this case, the XRD patterns of the powders (Fig. 3) reveal the persistence of $BaCO_3$ phase. Logically, theTiO_2 phase is not visible anymore. The XRD patterns do not show the presence of any other oxide containing barium. Finally, the powder was washed in nitric acid solution, to eliminate the excess of carbonate, and then dried for one night at 80 °C. The pH of the washing solution was chosen to be ~ 5 to avoid the dissolution

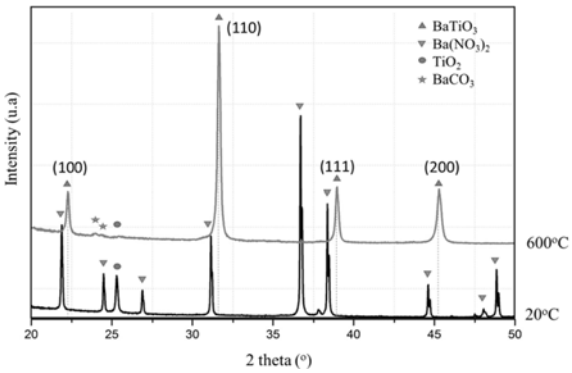

Fig. 2. XRD patterns of powders: 8hrs milled mixture BN and TiO_2 before and after calcination (1 hr, 600 °C).

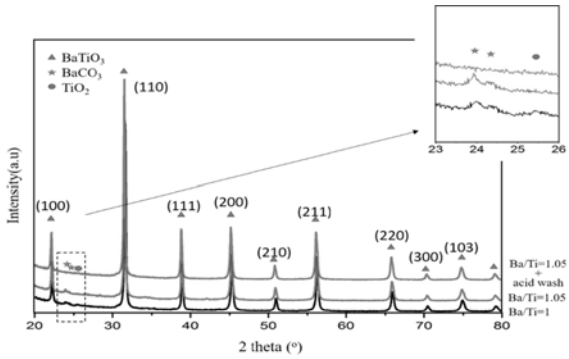

Fig. 3. XRD patterns of powders 8 hrs milled and calcined (1 hr, 600 °C): stoichiometric BN and TiO_2, and $Ba(NO_3)_2$ excess, BN and TiO_2 before and after acid wash.

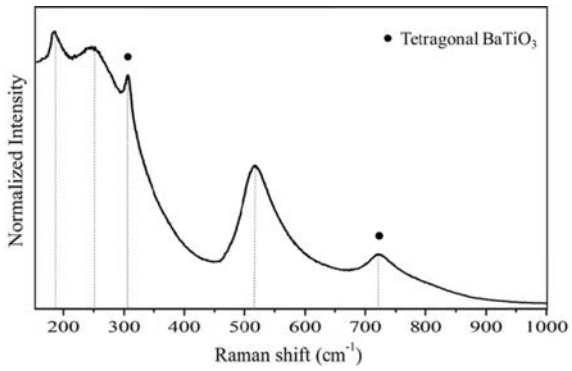

Fig. 4. Raman spectrum of $BaTiO_3$ (obtained by 8 hrs of milling at 350 rpm, and calcined 1hr at 600 °C.

of BT and to dissolve the $BaCO_3$ at the same time [29]. The XRD patterns of the washed and dried powder show a pure cubic perovskite barium titanate phase (Fig. 3).

The Raman spectra of the as synthesized pure barium titanate powder is shown in Fig. 4. The spectra consists in five peaks at 185, 250, 305, 515 and 720 cm^{-1}, which are characteristics of the tetragonal $BaTiO_3$ phase, contrary to what has been observed by XRD. Such unexpected difference has been observed by Hoshina et al. [29]. These authors, explained that, for very small BT particles (particle size between 20 and 30 nm), the average and static symmetries from XRD

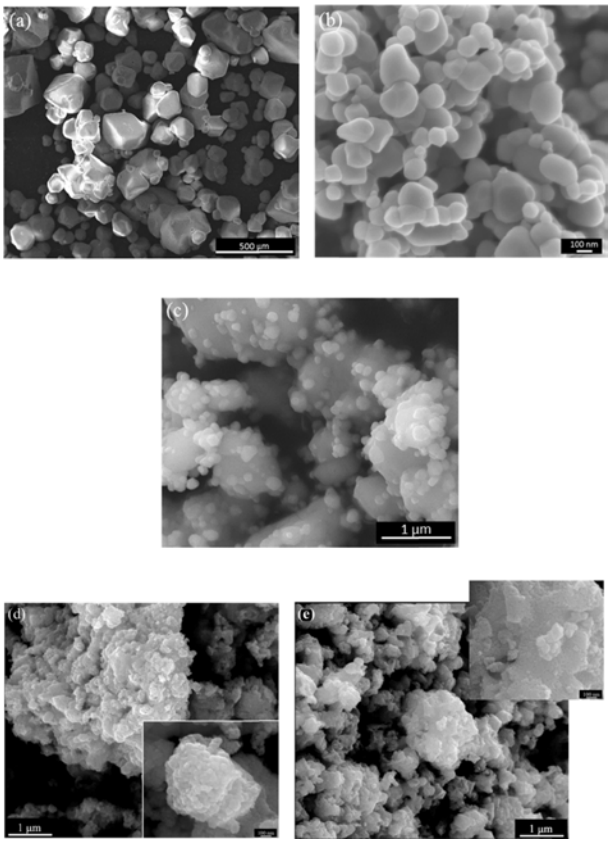

Fig. 5. SEM micrographs of: (a) commercial BN and (b) commercial TiO_2, (c) as milled mixture BN and TiO_2 and BT powders derived from calcination at 600 °C for 1 hr before (d) and after acid wash (e).

measurement were assigned to cubic BT, while the local and dynamic symmetries from Raman scattering measurement was assigned to tetragonal *P*4*mm*. This symmetry difference is similar to that of $BaTiO_3$ single crystals above Curie temperature T*c*. Therefore, the symmetry difference observed in BT particles whose grain size is lower than 30 nm finds its origin in the intrinsic phase transition behavior of $BaTiO_3$ [30].

The SEM-FEG observations were performed to understand the intermediate steps during the synthesis process (Fig. 5). Fig. 5(a) shows that the $Ba(NO_3)_2$ grains are sphere like with a grain size higher than 100 µm. Fig. 5(b) evidenced nanometric grain for the anatase TiO_2 powder. The grain size of $Ba(NO_3)_2$ clearly decreases after the 8hrs milling as shown in Fig. 5(c). After 1 hr of calcination at 600 °C, the big particles disappeared and the powder is made of agglomerated nanometric grains (~ 30 nm) (Fig. 5(d)). Finally, the acidic wash on the powder morphology (Fig. 5(e)). The grain size, determined from BET measurements, was approximately 240 nm, which confirms the agglomeration stage of the calcined powder. The aggregation phenomenon can be explained by two main reasons: First, nanoparticles generally have large surface area and high surface energy, and tend to

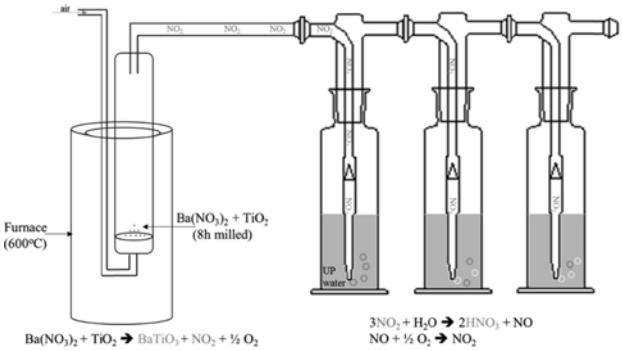

Fig. 6. Schematic representation of the process of NO_2 trapping during the calcination treatment.

reduce their surface energy by aggregating into larger agglomeration. Second, the calcination was carried out at a relatively high temperature (600 °C), which may cause the beginning of the sintering phenomenon.

The use of barium nitrate, as the barium source instead of barium carbonate, reduced the consumption of energy for the formation of BT (temperature and duration). However, nitrate precursors lead to the emission of toxic NOx gas:

$$Ba(NO_3)_2 + TiO_2 \rightarrow BaTiO_3 + 2NO_2 + ½\ O_2 \quad (3)$$

In other words, the gain of energy for the synthesis of BT creates an increase in of the toxicity during this process. This problem has been solved by using the system shown in the Fig. 6. The powder was calcinated under airflow and the other end of the system is connected to a gas bubbler filled by ultrapure water. Therefore, the released NO_2 is trapped in ultrapure water and the following reactions occur [31]:

$$3NO_2 + H_2O \rightarrow 2H + + 2NO^{-}_3 + NO \quad (4)$$

$$2NO_2\ N_2O_4 + H_2O \rightarrow HNO_3 + HNO_2 \quad (5)$$

$$NO_2 + NO\ N_2O_3 + H_2O \rightarrow 2HNO_2 \quad (6)$$

$$2HNO_2 \rightarrow HNO_3 + 2NO_2 + H_2O \quad (7)$$

$$NO + ½\ O_2 \rightarrow NO_2 \quad (8)$$

At the end of the BT synthesis, two solutions of nitric acid were obtained; the first one has a pH of 1, and the second a pH of 2. These homemade solutions were used for the washing of the powder, in order to get rid of the remaining carbonates.

The dense dielectrics ceramics were sintered by SPS at a temperature of 1112 °C and a pressure of 50 MPa. These conditions have been optimized in a previous work [32]. The sintered materials displayed a blue color due to the reducing sintering atmosphere. In all cases, a density of 97% is determined. The ceramics crystallize in the tetragonal structure (JCPDS files No.

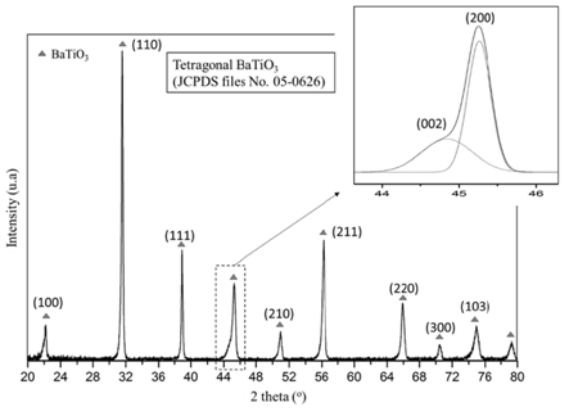

Fig. 7. XRD patterns of BT nanoceramic sintered by SPS.

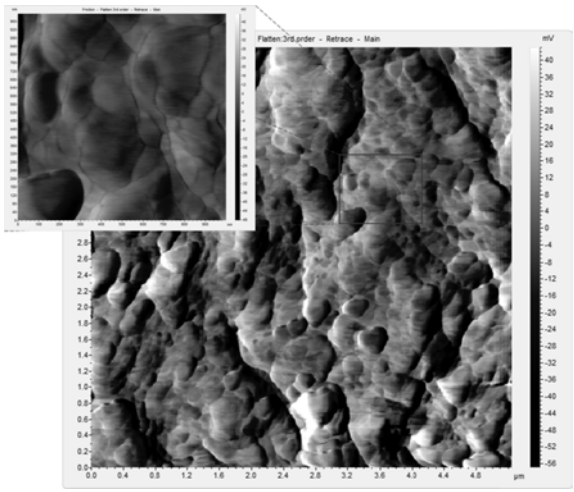

Fig. 8. AFM micrographs of a fracture of a BT nanoceramic sintered by SPS.

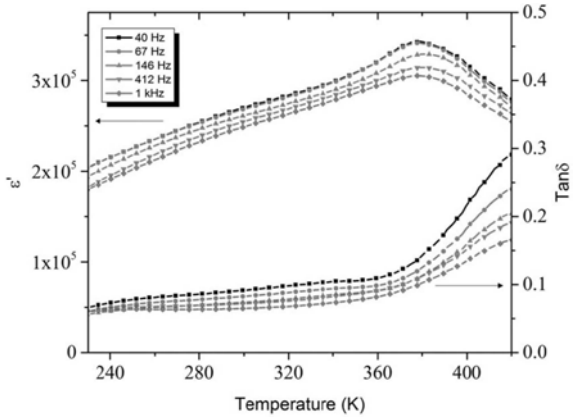

Fig. 9. Dielectric properties of a BT nanoceramic sintered by SPS, as a function of temperature (220-420 K) for different frequencies (40-1 KHz).

05-0626) (Fig. 7), highlighted by the splitting of the (200) peak at $2\theta = 44.5°$ (inset of Fig. 7). AFM micrographs (Fig. 8) of a cross section show no porosity. The grain size ranges from 200 to 400 nm.

The as sintered ceramics present high dielectric permittivity but also high dielectric losses induced by the presence of a high number of charge carriers, due to the reduction of Ti^{4+} in Ti^{3+} during the SPS sintering. An annealing/oxidation procedure was necessary to relieve residual stresses, eliminate oxygen vacancies (produced during the SPS procedure) and obtain a capacitive behavior. Voisin et al. [33] have optimized the annealing procedure in order to keep a colossal permittivity associated with low losses. The authors explained this behavior by a core shell structure made of semi conductive grains and insulating grain boundaries, due to the presence of Ti^{3+}, Ti^{4+} and oxygen vacancies. In the present case, the ceramics were annealed at 750 °C for 15 min.

Fig. 9 shows the dielectric permittivity (ε) and loss tangent (tgδ) variation with temperature, for different frequencies of the post-annealed nanostructured $BaTiO_3$ ceramic. It is worth noting that, at room temperature and a frequency of 1 kHz, the permittivity value $\varepsilon' = 2.5 \times 10^5$ can be named as colossal, while the value of the dielectric losses ($tg\ \delta = 0.07$) is still low. These electrical properties are very interesting, compared to the few data published in the literature. For instance, Alves et al. [16] have reported a permittivity of 3000 (at 300 K and 1 kHz) and $tg\ \delta = 0.02$ for $BaTiO_3$ ceramics sintered by SPS of powder derived from mechanically activated mixture of $BaCO_3$ and TiO_2. Whatever the frequency, the dielectric permittivity increases linearly with increasing temperature and reaches a maximum of 3.5×10^5 at 380 K, corresponding to the Curie temperature, and then decreases. It is clear that the T_C is shifted to a lower value than the one of conventionally sintered BT (Tc~ 400 K). The 20 degrees difference shows that the present sample is oxygen-deficient, as it is well known that Tc drops with oxygen loss. The dielectric losses remain in an acceptable range whatever the frequency and temperature ranges.

Conclusions

Cubic structured barium titanate nanoparticles were obtained by simple ball milling of $Ba(NO_3)_3$ and TiO_2 followed by calcination at 600 °C during 1 hr. The obtained powders show a particle size of ~ 30 nm with a crystallite size of ~ 25 nm. High density ceramics (densification > 98%) were successfully obtained by SPS. The dense ceramics have nanoscale grains and tetragonal structure. Colossal permittivity up to 2.5×10^5 and low losses (0.07) have been measured at 300 K and 1 kHz.

Acknowledgments

This work was supported by the Lebanese National Center for Scientific Research, the tow doctoral school of Lebanese university (doctoral school of science and technology EDST) and Paul Sabatier III University in Toulouse (doctoral school of material sciences SDM).

References

1. W. Heywang, J. Am. Ceram. Soc. 47 (1964) 484-490.
2. J.M. Herbert, A.J. Moulson, Electroceramics: Materials, Properties, Applications, 2nd Edition, Chapman and Hall, London (2003).
3. Y. Ohara, K. Koumoto, H. Yanagida, J. Am. Ceram. Soc. 68 (1985) C-108-C-109.
4. M.T. Buscaglia, M. Bassoli, V. Buscaglia, R. Alessio, J. Am. Ceram. Soc. 88 (2005) 2374-2379.
5. H. Xu, L. Gao, Mater. Lett. 58 (2004) 1582-1586.
6. S.K. Lee, G.J. Choi, U.Y. Hwang, K.K. Koo, T.J. Park, Mater. Lett. 57 (2003) 2201-2207.
7. W. Li, Z. Xu, R. Chu, P. Fu, J. Hao, J. Alloys Compd. 482 (2009) 137-140.
8. R. Kavian, A. Saidi, J. Alloys Compd. 468 (2009) 528-532.
9. L. Wu, M.-C. Chure, K.-K. Wu, W.-C. Chang, M.-J. Yang, W.-K. Liu, M.-J. Wu, Ceram. Int. 35 (2009) 957-960.
10. Z. Valdez-Nava, S. Guillemet-Fritsch, C. Tenailleau, T. Lebey, B. Durand, J.Y. Chane-Ching, J. Electroceram. 22 (2009) 238-244.
11. R. Licheri, S. Fadda, R. Orrù, G. Cao, V. Buscaglia, J. Eur. Ceram. Soc. 27 (2007) 2245-2253.
12. C. Gomez-Yañez, C. Benitez, H. Balmori-Ramirez, Ceram. Int. 26 (2000) 271-277.
13. L.B. Kong, J. Ma, H. Huang, R.F. Zhang, W.X. Que, J. Alloys Compd. 337 (2002) 226-230.
14. S. Ohara, A. Kondo, H. Shimoda, K. Sato, H. Abe, M. Naito, Mater. Lett. 62 (2008) 2957-2959.
15. A.K. Nath, C. Jiten, K.C. Singh, Physica B: Condensed Matter 405 (2010) 430-434.
16. M.F.S. Alves, R.A.M. Gotardo, L.F. Cótica, I.A. Santos, W.J. Nascimento, D. Garcia, J.A. Eiras, cripta Mater. 66 (2012) 1053-1056.
17. B.D. Stojanovic, A.Z. Simoes, C.O. Paiva-Santos, C. Jovalekic, V.V. Mitic, J.A. Varela, J. Eur. Ceram. Soc. 25 (2005) 1985-1989.
18. H.A.M. van Hal, W.A. Groen, S. Maassen, W.C. Keur, J. Eur. Ceram. Soc. 21 (2001) 1689-1692.
19. L.G.D. Silveira, M.F.S. Alves, L.F. Cótica, R.A.M. Gotardo, W.J. Nascimento, D. Garcia, J.A. Eiras, I.A. Santos, Mater. Res. Bull. 48 (2013) 1772-1777.
20. T. Sundararajan, S.B. Prabu, S.M. Vidyavathy, Mater. Res. Bull. 47 (2012) 1448-1454.
21. V. Berbenni, A. Marini, G. Bruni, Thermochim. Acta 374 (2001) 151-158.
22. S.-S. Ryu, S.-K. Lee, D.-H. Yoon, J. Electroceram. 18 (2007) 243-250.
23. J. Xue, J. Wang, D. Wan, J. Am. Ceram. Soc. 83 (2000) 232-234.
24. D.-H. Yoon, Journal of Ceramic Processing Research **7[**4] (2006) 343-354.
25. S. Guillemet-Fritsch, Z. Valdez-Nava, C. Tenailleau, T. Lebey, B. Durand, J.Y. Chane-Ching, Adv. Mater. 20 (2008) 551-555.
26. H. Han, C. Voisin, S. Guillemet-Fritsch, P. Dufour, C. Tenailleau, C. Turner, J.C. Nino, J. Appl. Phys. 113 (2013) 024102.
27. E. Brzozowski, M.S. Castro, Thermochim. Acta 398 (2003) 123-129.
28. B. Chen, F.-H. Liao, H. Jiao, X.-P. Jing, Phase Transitions 86 (2012) 380-390.
29. A. Neubrand, R. Lindner, P. Hoffmann, J. Am. Ceram. Soc. 83 (2000) 860-864.
30. T. Hoshina, H. Kakemoto, T. Tsurumi, S. Wada, M. Yashima, J. Appl. Phys. 99 (2006) 054311.
31. R. Burlica, B.R. Locke, IEEE Transactions on 44 (2008) 482-489.
32. T. Al-Naboulsi, M. Boulos, C. Tenailleau, P. Dufour, M. Zakhour, S. Guillemet-Fritsch, International Journal of Engineering Research & Science 1 (2015).
33. C. Voisin, S. Guillemet-Fritsch, P. Dufour, C. Tenailleau, H. Han, J.C. Nino, Int. J. Appl. Ceram. Technol. 10 (2013) E122-E133.